EDGE ARTICLE

Check for updates

Ligand-engineered synthesis of carbon encapsulated Ni nanoparticles for efficient alkaline hydrogen oxidation reaction

Yanan Chen,[a] Aiqing Cao,[b] Yongsheng Wang,[a] Jiaxin Wang,[a] Hao Wang,[a] Qingqing Lv,[a] Shuxin Zhang,[a] Chengjin Chen,[a] Yaping Li, [ID][b] Wei Zhu [ID] *[ac] and Zhongbin Zhuang [ID] *[ac]

The development of high performance non-precious metal-based hydrogen oxidation reaction (HOR) catalysts under alkaline conditions is important for achieving low cost hydroxide exchange membrane fuel cells (HEMFCs). Herein, we report a high performance Ni-based HOR catalyst through engineering of the ligand of its precursor. Carbon encapsulated Ni nanoparticles are synthesized through pyrolysis of the Ni complex. It is found that the nitrogen content in the ligands determines the nitrogen doping level in the final catalysts, which controls the hydrogen binding energy of the catalysts. The position of functional groups in the ligands regulates the electronic state of Ni, which controls the metallic Ni content in the final catalysts. Ni-Py-3-AO synthesized using pyridine-3-amidoxime as the ligand achieves a high HOR exchange current density of 138 $\mu A\ cm_{Ni}^{-2}$ and a mass activity of 94.1 A g_{Ni}^{-1} at 50 mV of overpotential. A high peak power density of 554 mW cm^{-2} is achieved for the HEMFC using Ni-Py-3-AO as the anode. Mechanistic studies reveal that its superior HOR activity originates from modulated hydrogen binding energy as well as well-structured interfacial water.

Introduction

Hydroxide exchange membrane fuel cells (HEMFCs, also known as anion exchange membrane fuel cells, AEMFCs) represent an emerging fuel cell technology that employs hydroxide ion-conducting membranes to achieve efficient energy conversion in alkaline environments.[1] Compared with proton exchange membrane fuel cells (PEMFCs), HEMFCs offer the advantage of compatibility with non-precious metal catalysts as well as stainless steel bipolar plates, significantly reducing the costs.[2,3] With the development of high performance hydroxide exchange membranes, the performance of state-of-the-art HEMFCs rivals the performance of PEMFCs. However, high performance HEMFCs still rely on platinum group metal catalysts.[4] Especially for the anodic hydrogen oxidation reaction (HOR), its kinetics on the platinum group metal catalysts in alkaline electrolyte is 2–3 orders of magnitude lower than that in acidic electrolyte, making a much higher anode platinum group metal loading

requirement for HEMFCs than that for PEMFCs.[5,6] Consequently, developing high-performance non-precious metal based HOR catalysts is essential for realizing the low cost of HEMFCs.

Nickel-based HOR catalysts have emerged as promising candidates for replacing platinum group metals under alkaline conditions.[7,8] However, the intrinsic HOR activity and stability of Ni lag behind that of platinum group metals. The HOR activity of Ni typically reaches only 1/1000 to 1/100 of the activity of Pt.[9] The unsatisfactory HOR activity of Ni stems primarily from Ni's overly strong hydrogen binding energy (HBE),[10] which slows down the Volmer step kinetics. Recent studies also suggest that the hydroxide adsorption strength and the interfacial water structures have a significant impact on the HOR kinetics under alkaline conditions.[11–13] Efforts have been made to optimize these properties to improve the HOR kinetics of Ni-based catalysts, by alloying,[14–16] heteroatom doping,[17–20] support interface engineering,[21–23] encapsulation,[24–27] *etc.* For example, Li *et al.* demonstrated that alloying Ni with Mo can effectively weaken HBE,[16] and enhance the adsorption of hydroxyl species, leading to an enhanced HOR activity. Yan *et al.* demonstrated that the HBE of Ni could be tuned by the support, and the N-doped carbon nanotube-supported Ni nanoparticles illustrate high HOR activity.[17] Wang *et al.* demonstrated that the metallic Ni and $MoBT_x$ MBene ($Ni/MoBT_x$) heterostructure catalyst exhibits high HOR activity through the metal–support interaction to achieve modulated HBE.[22] Recent advances show that

[a] *State Key Lab of Organic-Inorganic Composites, Beijing Advanced Innovation Center for Soft Matter Science and Engineering, Beijing University of Chemical Technology, Beijing, 100029, China. E-mail: zhuwei@mail.buct.edu.cn; zhuangzb@mail.buct.edu.cn*

[b] *State Key Laboratory of Chemical Resource Engineering, College of Chemistry, Beijing University of Chemical Technology, Beijing, 100029, China*

[c] *Beijing Key Laboratory of Intelligent Design and Manufacturing for Hydrogen Energy Materials, Beijing University of Chemical Technology, Beijing, 100029, China*

encapsulated Ni nanoparticles have confined surface structures with adjusted HBE as well as enhanced stability, illustrating high promise for the HOR.[28–31] Hu *et al.* reported Ni nanoparticles embedded within nitrogen-doped carbon to reach balanced hydrogen and hydroxide binding, exhibiting an electrochemically active surface area-normalized exchange current density of 70 $\mu A\ cm^{-2}$ and a peak power density of 628 mW cm^{-2} in the HEMFC test.[32] Zhuang *et al.* synthesized a Ni@C core–shell catalyst *via* controlled H_2/Ar annealing of Ni_2EDTA precursors.[33] By controlling the etching of the carbon shell, high HOR activity is achieved. Wei *et al.* confined Ni nanoparticles within carbon-doped-MoO_x/MoO_x, which exhibits a quantum well-like structure and can selectively transfer external electrons from the HOR while remaining metallic, resulting in high activity and stability.[34]

Here, we report carbon encapsulated Ni nanoparticles synthesized by pyrolysis of a Ni complex. Six different ligands are employed to synthesize the Ni complex, and their impacts on the HOR performances are studied. It is found that the nitrogen content in the ligands and the position of the functional groups are important. The catalyst obtained by using pyridine-3-amidoxime as the ligand (Ni-Py-3-AO) achieves a high HOR performance with an exchange current density of 138 μA cm_{Ni}^{-2} and a mass activity of 94.1 A g^{-1} at 50 mV. By using Ni-Py-3-AO as the anode, the fabricated HEMFC delivers a high peak power density of 554 mW cm^{-2}, surpassing most reported HEMFCs using non-precious metal based anodes. The high HOR activity is attributed to its optimized HBE and regulated interfacial water structures. These results illustrate that high performance HOR catalysts could be synthesized by regulating the coordination structure of the precursor.

Results and discussion

Synthesis and characterization of catalysts

A pyrolysis method is employed to synthesize the Ni based catalysts. Ni complex precursors are synthesized first, and then pyrolyzed at high temperature to obtain the catalysts (Fig. 1a). By selecting different ligands, the structures of the obtained Ni-based catalysts are regulated, and the HOR performances are modulated. In order to understand the ligand structure–HOR performance relationship, a series of ligands are studied.

Due to the strong coordinating ability of the N-related groups, nitrogen heterocycle compounds are selected as the ligands, and the structures of the ligands used are listed in Fig. 1a. The N atoms in the ligands may maitain in the pyrolyzed carbon products, resulting in N doped catalysts and providing tuning effects. Amidoxime, amino and oxime groups are further connected on the nitrogen heterocycle to provide multiple sites to coordinate with Ni^{2+}. Pyridine functionalized with amidoxime is employed, and the positional isomerism of functional groups on aromatic rings (*i.e.*, pyridine-2-amidoxime (Py-2-AO), pyridine-3-amidoxime (Py-3-AO), and pyridine-4-amidoxime (Py-4-AO)) is employed to study the geometric effect of the ligands. Pyrazine functionalized with amidoxime (pyrazine-2-amidoxime (Pa-3-AO)) is used to study the effect of additional N in the heterocycle. Additionally, pyridine functionalized with aldoxime

(pyridine-3-aldoxime (Py-3-O)) is employed as a control to elucidate the effect of the amino group on the oxime. 2-Aminopyridine-3-carbaldehyde oxime hydrochloride (Py-2A-3O), with both amino and aldoxime substitutions on the pyridine, is also employed to study the effect of the position of the amino group. The catalysts obtained by using the corresponding Ni complex are named Ni-ligand, where the abbreviations of the ligands are used.

The X-ray diffraction (XRD) patterns are shown (Fig. 1b) for the catalysts obtained by pyrolysis of precursors with different ligands. Metallic Ni is observed for all the catalysts, indicated by the characteristic peaks at 44.4°, 51.8°, and 76.4° corresponding to the Ni(111), (200), and (220) facets, respectively. The broad peak at 26° arises from carbon, suggesting that carbon residue also exists in the catalysts. Transmission electron microscopy (TEM) analysis (Fig. 1c) reveals that all the catalysts are Ni nanoparticles encapsulated with carbon. However, the size of the Ni nanoparticles as well as the morphologies of the encapsulated carbon are different for the catalysts synthesized using different ligands, indicating the important role of the ligands. For Ni-Py-3-AO, Ni-Py-2-AO, Ni-Py-4-AO and Ni-Pa-3-AO, small nanoparticles supported on carbon are obtained. For Ni-Py-3-AO, uniform Ni nanoparticles with an average size of 6.6 nm (size distribution shown in Fig. S1a) are obtained, and the nanoparticles are evenly distributed on carbon supports. The sizes of the Ni nanoparticles are larger, with an average size of 11.8 nm, 13.1 nm and 9.4 nm for Ni-Py-2-AO, Ni-Py-4-AO and Ni-Pa-3-AO, respectively (Fig. 1d–f and S1b–d). In contrast, for Ni-Py-3-O, large Ni nanoparticles with a size of hundreds of nanometers (Fig. 1g and S1e) are supported on carbon. For Ni-Py-2A-3O, the particle size is smaller (Fig. 1h and S1f), but a large amount of carbon residue exists and the nanoparticles are embedded in the carbon substrates. The particle sizes of the catalysts are also estimated using the Debye–Scherrer formula based on the XRD data, and are summarized in Table S1. The particle sizes calculated from the XRD pattern are in agreement with the sizes observed in TEM images.

The carbon residue in the products is characterized using Raman spectra (Fig. S2). The carbon related Raman peaks could be divided into 4 categories: the D1 band at ~1350 cm^{-1}, attributed to A_1g breathing mode related to structural defects; the D3 band at ~1500 cm^{-1}, attributed to tetrahedral amorphous carbon from organic molecules and fragments; the D4 band at ~1181 cm^{-1}, attributed to sp^3-hybridized carbon/surface functional groups; and the G band at 1580 cm^{-1}, attributed to graphitic carbon.[35,36] It is found that the defects in the carbon, which are represented by the intensity ratio I_{D1}/I_G, are controlled by the number of heteroatoms in the ligands. Using Py-3-O, which contains 2 N and 1 O, the product Ni-Py-3-O has a low I_{D1}/I_G of 2.00. Using the ligands with 3 N and 1 O, the products show the I_{D1}/I_G of 2.14, 2.16, 2.25 and 2.12 for Ni-Py-2-AO, Ni-Py-3-AO, Ni-Py-4-AO, and Ni-Py-2A-3O, respectively. Pa-2-AO has 4 N and 1 O, resulting in the highest I_{D1}/I_G of 2.69 for the obtained Ni-Pa-2-AO. The amount of the incompletely pyrolyzed ligands is determined by the I_{D3}/I_G ratio.

For Ni-Pa-3-AO and Ni-Py-3-O, they show high I_{D3}/I_G of 1.13 and 0.93, respectively. The incompletely pyrolyzed ligands may
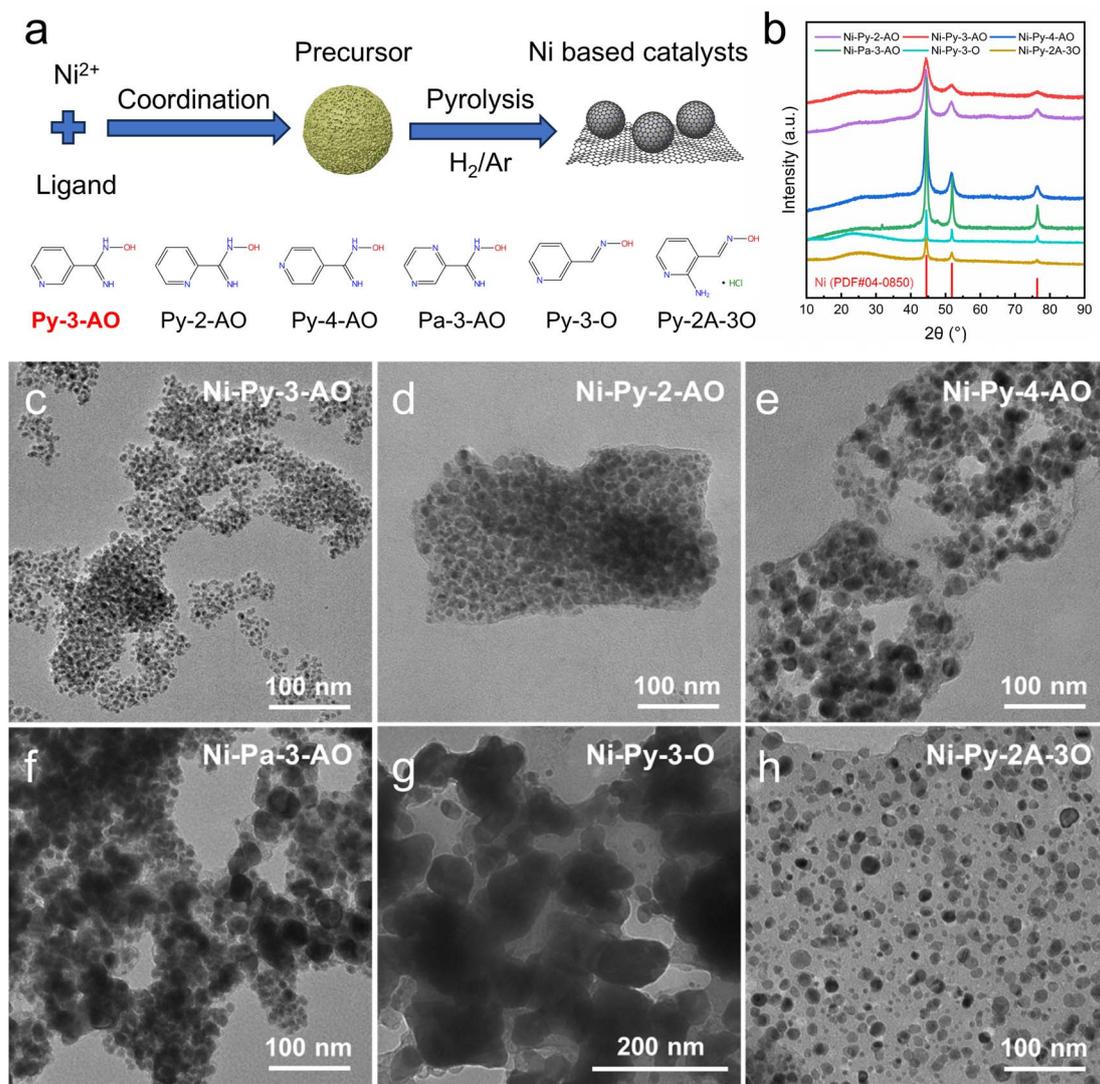
Fig. 1 (a) Schematic illustration of the synthetic procedure. (b) XRD patterns of the catalysts. (c–h) TEM images of the catalysts. (c) Ni-Py-3-AO, (d) Ni-Py-2-AO, (e) Ni-Py-4-AO, (f) Ni-Pa-3-AO, (g) Ni-Py-3-O and (h) Ni-Py-2A-3O.

block the active sites, resulting in decreased catalytic activity. Ni-Py-3-AO is taken as an example for detailed analysis. The high-resolution transmission electron microscopy (HRTEM) image of Ni-Py-3-AO (Fig. 2a) reveals well-defined lattice fringes with an interplanar spacing of 0.206 nm corresponding to the Ni(111) facet. The nanoparticles are encapsulated by few-layer carbon shells with a characteristic spacing of 0.34 nm, consistent with the graphite (002) facet. Elemental mapping *via* EDS (Fig. S3) confirms the presence of Ni, C, N, and O throughout the catalyst. HAADF-STEM analysis (Fig. 2b) further demonstrates homogeneous dispersion of Ni nanoparticles on a uniformly distributed carbon matrix, with N and O species predominantly localized at nanoparticle peripheries. Ni mass content is 64% in Ni-Py-3-AO measured by ICP-MS.

HOR activity of catalysts

Catalyst performance for the HOR was evaluated using a rotating disk electrode in H_2-saturated 0.1 M KOH. The Ni/C

catalyst synthesized *via* an impregnation method was tested for comparison (TEM image shown in Fig. S4).[14] Clear anodic current is observed when using Ni-Py-3-AO, Ni-Py-2-AO and Ni-Py-4-AO as the catalysts, and the current densities are higher than that using Ni/C (Fig. 3a). Ni-Pa-3-AO shows similar activity to that of Ni/C, while Ni-Py-3-O and Ni-Py-2A-3O show worse activity than that of Ni/C. The kinetic current densities are worked out using the Koutecký–Levich equation and summarized in Table S2. Ni-Py-3-AO displays the highest activity, indicated by the rapid increase of the current density with potential. Its activity approaches that of Pt/C with lower loadings (Fig. S5). The anodic current disappears when switching the electrolyte to an Ar-saturated one, confirming that the anodic current observed in the H_2-saturated electrolyte originates from the HOR (Fig. S6). Fig. S7 and S8 show the Koutecký–Levich plots of the current density at 25 mV obtained at various rotating speeds, and the slope is 4.68 cm^2 mA^{-1} $s^{1/2}$, consistent
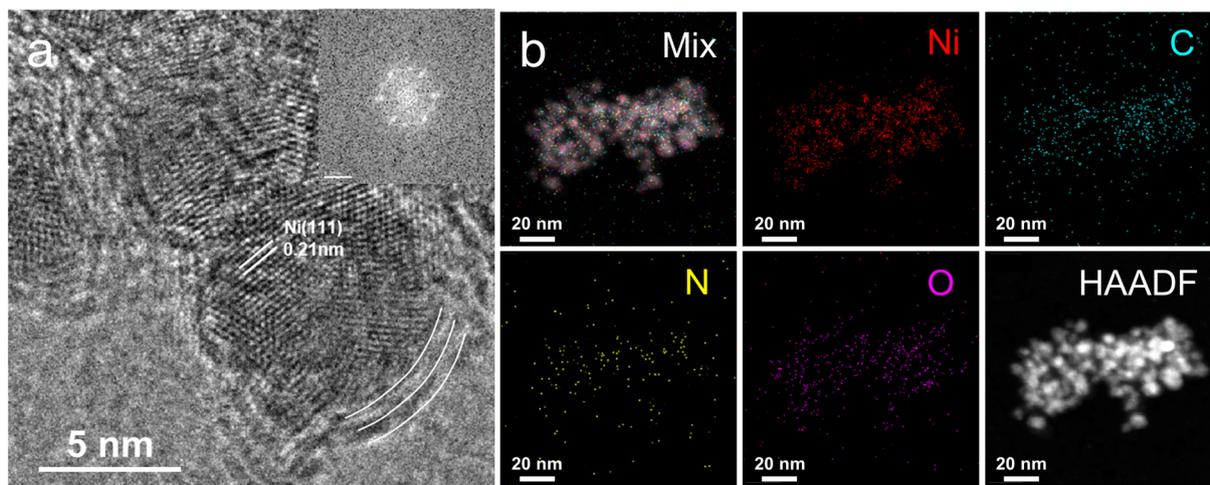
Fig. 2 (a) HAADF-STEM image of Ni-Py-3-AO. (b) HAADF-EDS mapping of Ni-Py-3-AO.

with the theoretical value of 4.87 cm^2 mA^{-1} s$^{1/2}$ for the two-electron transfer HOR process.

To understand the intrinsic activities of the catalysts, the mass activities using HOR kinetic current densities ($j_{k,m}$) at 50 mV (*versus* RHE, the same hereafter) and the electrochemically active surface area (ECSA) normalized exchange current densities ($j_{0,s}$) are calculated. The ECSA is estimated through the charge integration during the Ni(OH)$_2$ reduction to Ni (Fig. S9).
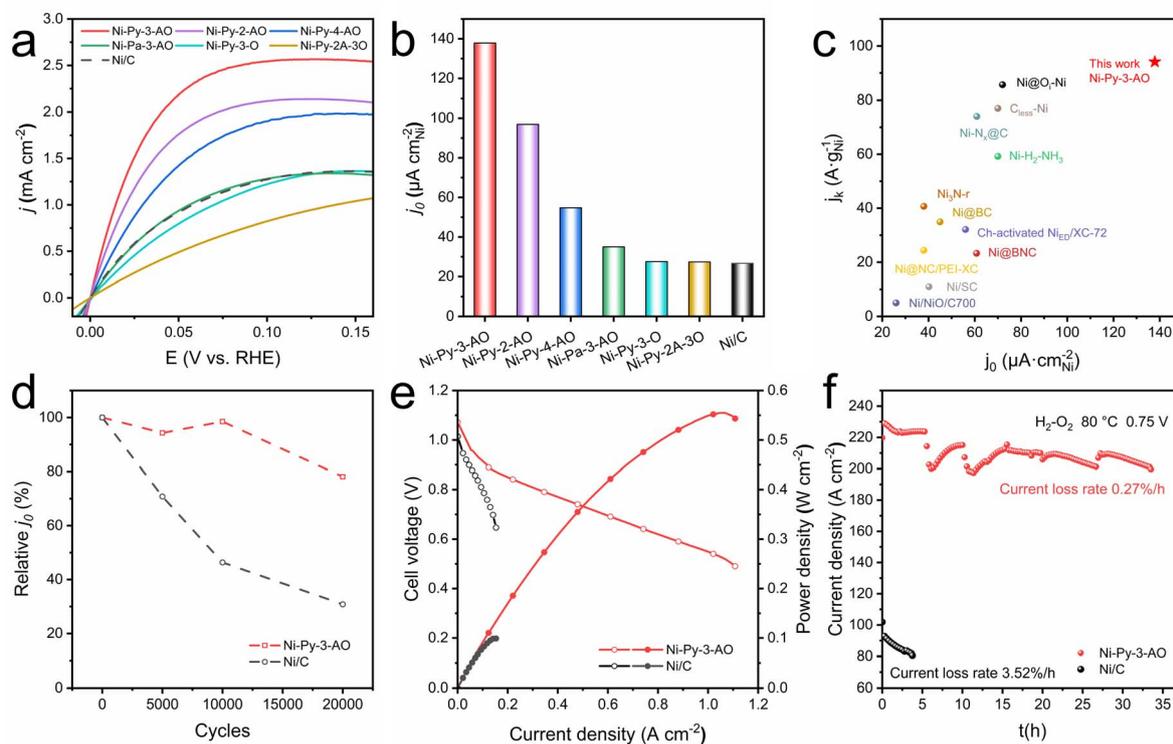

Fig. 3 (a) Polarization curves of the catalysts in H$_2$-saturated 0.1 M KOH solution with a rotation rate of 1600 rpm and a scan rate of 1 mV s^{-1}. The catalyst loading was 230 μg$_{cat}$ cm^{-2}. The potentials were *iR* corrected. (b) The specific exchange current density ($j_{0,s}$). (c) Summary of the $j_{0,s}$ and $j_{k,m}$ at 50 mV for Ni-Py-3-AO and the reported Ni-based single metal catalysts. (d) The relative exchange current density evolution in the ADT test of Ni-Py-3-AO and Ni/C tested in H$_2$-saturated 0.1 M KOH with a rotation rate of 1600 rpm. (e) H$_2$/O$_2$ HEMFC performances using Ni-Py-3-AO or Ni/C as the anode catalyst. The anode Ni loading was controlled at 4 mg$_{Ni}$ cm^{-2}. The cathode for all the HEMFCs was 0.4 mg$_{Pt}$ cm^{-2} Pt/C. The cell, anode and cathode humidifier temperatures were 95, 92 and 95 °C, respectively. The anode and cathode were supplied with 0.5 L min^{-1} of H$_2$ and 0.5 L min^{-1} of O$_2$, respectively. The backpressure was 250 kPaG for both sides. (f) H$_2$/O$_2$ HEMFC durability test at a constant current density of 0.75 V with Ni-Py-3-AO (3 mg$_{Ni}$ cm^{-2}) or Ni/C as the anode and Pt/C (0.4 mg$_{Pt}$ cm^{-2}) as the cathode. Test conditions: the cell, anode and cathode humidifier temperatures were 80, 78 and 80 °C, respectively. The anode and cathode were supplied with 0.3 L min^{-1} of H$_2$ and 0.3 L min^{-1} of O$_2$, respectively. The backpressure was 100 kPa for both sides.

The exchange current densities are fitted using the Butler–Volmer equation (Fig. S10) and summarized in Fig. 3b and Table S2. Ni-Py-3-AO achieves a high $j_{k,m}$ of 94.1 A g^{-1} and $j_{0,s}$ of 138 μA cm$_{Ni}^{-2}$, which are 10.8-fold and 5.2-fold higher compared with that of Ni/C ($j_{k,m}$ = 8.7 A g^{-1}; $j_{0,s}$ = 27 μA cm$_{Ni}^{-2}$). Ni-Py-2-AO, Ni-Py-4-AO, and Ni-Pa-3-AO exhibit $j_{0,s}$ of 97, 55, and 35 μA cm$_{Ni}^{-2}$, respectively. They are lower than that for Ni-Py-3-AO but better than that for Ni/C. Ni-Py-3-O and Ni-Py-2A-3O exhibit $j_{0,s}$ of about 27 μA cm$_{Ni}^{-2}$, similar to that of Ni/C. This demonstrates that no advantage is gained by using Py-3-O and Py-2A-3O as the ligands. Ni-Py-3-AO positions itself as the highest-performing nickel-based single metal HOR catalyst reported (Fig. 3c and Table S3).

The stability of Ni-Py-3-AO is estimated by accelerated degradation testing (ADT) by cycling between −0.05 and 0.1 V at a scan rate of 0.1 V s^{-1}, and chronoamperometry (CA) at 50 mV in H$_2$-saturated 0.1 M KOH. Fig. S11–S14 show the polarization curves for Ni-Py-3-AO and Ni/C after 0, 5000, 10 000 and 20 000 ADT cycles, and Fig. 3d summarizes the calculated exchange current densities. Ni-Py-3-AO retains 78.1% of its initial exchange current density after 20 000 ADT cycles, much better than that for Ni/C (30.8%). The CA curves for Ni-Py-3-AO and Ni/C are shown in Fig. S15. After 50 h of testing, the relative current density decays by only 20% for Ni-Py-3-AO. By comparison, Ni/C suffers 20% of degradation within 5 h. The calculated decay rate for Ni-Py-3-AO is only 0.39% h^{-1}, which is an order of magnitude lower than that of Ni/C (4% h^{-1}). Moreover, post-stability characterization confirms that Ni-Py-3-AO retains its original morphological structure (Fig. S16 and S17). These results demonstrate the much-improved stability of Ni-Py-3-AO compared with that of Ni/C.

Membrane electrode assemblies (MEAs) were fabricated using Ni-Py-3-AO or Ni/C (3 mg$_{Ni}$ cm^{-2}) as the anode catalyst and commercial 40% Pt/C (0.4 mg$_{Pt}$ cm^{-2}) as the cathode. Fig. 3e shows the polarization curves as well as the power density curves. The Ni-Py-3-AO HEMFC displays an open-circuit voltage of 1.06 V. Its peak power density reached 554 mW cm^{-2}, which is much higher than that of the Ni/C HEMFC (99 mW cm^{-2}). The peak power density of the Ni-Py-3-AO HEMFC exceeds the values of most reported HEMFCs using Pt-free anodes (Table S4). Additionally, the Ni-Py-3-AO HEMFC can deliver a current density of 428 mA cm^{-2} at 0.65 V, which is also higher than that of Ni/C (153 mA cm^{-2}). The Ni-Py-3-AO HEMFC also shows enhanced stability compared with the Ni/C HEMFC. Fig. 3f shows the current density curves of the HEMFC working at 0.75 V. The Ni-Py-3-AO HEMFC shows an average decay rate of 0.27% h^{-1}, in a 35 h test. In contrast, the Ni/C HEMFC shows a much higher decay rate of 3.5% h^{-1}. The fluctuation of the current density in the stability test might result from temporal flooding.

Theoretical calculations and mechanism investigation

The HOR proceeds through the activation of the H$_2$ molecules to form adsorbed hydrogen (*H), followed by electron transfer and combination with OH$^-$ to complete the reaction. The binding energy of the key intermediate *H (i.e., hydrogen binding energy, HBE) is considered to control the kinetics of the HOR, in the form

of the well-established HBE volcano plot.[10] Ni is located on the branch with too strong HBE; therefore, the weakened HBE of the catalysts benefits improvement of the HOR activity. Beyond HBE, the interfacial water structure is also found to be important for the HOR under alkaline conditions. The hydrogen-bonding network is a well-structured network that facilitates efficient proton–electron transfer.[11,12] The transfer of hydrogen from the bulk solution to the electrode surface to form *H strongly depends on the orientation of interfacial water molecules and the integrity of the hydrogen-bonding network. A well-structured hydrogen-bonding network can lower the energy barrier for proton transfer, thereby accelerating the reaction.[35] Conversely, a disrupted network impedes proton transfer, thereby hindering the HOR process.

The chemical environments of the Ni nanoparticles in the catalysts are investigated by XPS. Fig. 4a shows the high resolution Ni 2p$_{3/2}$ XPS spectra of the 4 HOR catalysts with higher HOR activity (i.e., Ni-Py-2-AO, Ni-Py-3-AO, Ni-Py-4-AO, and Ni-Pa-3-AO), as well as Ni/C for comparison. For the 4 pyrolyzed catalysts, a peak located at 852.9 eV corresponding to Ni^0 species and a peak located approximately at 855 eV corresponding to Ni^{2+} species are observed. Compared with the Ni^0 peak for Ni/C (853.3 eV), the peaks exhibit a negative shift of approximately 0.4 eV, suggesting that the N-doped carbon shell modulates the electronic structure of Ni.

The peak positions of the Ni^0 species of these four catalysts do not show significant differences, indicating their similar chemical environments. However, the highest Ni^0 content (38%) is observed for Ni-Py-3-AO compared with Ni-Py-2-AO (32%), Ni-Py-4-AO (30%) and Ni-Pa-3-AO (28%). Due to the metallic Ni being generally considered as the active sites for the HOR, the highest Ni^0 content of Ni-Py-3-AO is attributed to its best HOR performance. The highest Ni^0 content of Ni-Py-3-AO is likely to originate from its precursor structures. Fig. S18 shows the high resolution Ni 2p$_{3/2}$ XPS spectra of the corresponding precursors of the 4 catalysts. It is found that the Ni 2p binding energy of the precursors is determined by the structure of the ligands, especially the position of the functional groups. The Ni-Py-3-AO precursor displays the lowest Ni 2p binding energy, indicating the coordination-induced electron donation from heteroatoms to Ni^{2+}. A correlation between the Ni 2p binding energy in the precursor and Ni^0 content in the final pyrolyzed catalysts is found (Fig. S19). The increased electron density of Ni^{2+} in the Ni-Py-3-AO precursor promotes the formation of metallic Ni^0 during pyrolysis, resulting in the highest Ni^0 content in Ni-Py-3-AO.

As demonstrated by the HRTEM images, the Ni nanoparticles are capped within carbon shells. It has been reported that the carbon shell influences the adsorption of the *H intermediates, thereby tuning the HBE. The composition of the carbon shell correlates with the HBE. The N 1s XPS spectrum of the catalysts demonstrates that the carbon shells are doped with N (Fig. 4b). The deconvolution results indicate that pyridinic N dominates the nitrogen species. The pyridinic N content in the carbon shell differs among the catalysts. For the two catalysts with higher HOR activities (i.e., Ni-Py-2-AO and Ni-Py-3-AO), the pyridinic N contents are approximately 5 at%. And
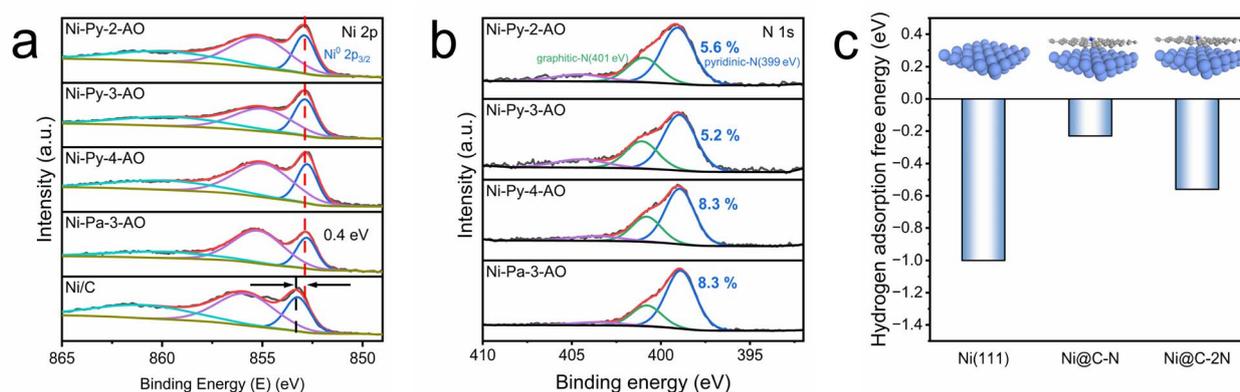
Fig. 4 High resolution XPS spectra of (a) Ni 2p$_{3/2}$ and (b) N 1s. (c) The hydrogen adsorption free energy on the Ni(111) surface, Ni@C−N, and Ni@C−2N.

for the two catalysts with moderate HOR activities (Ni-Py-4-AO and Ni-Pa-3-AO), the pyridinic N contents are approximately 8 at%. To understand the role of carbon and N doping in the HOR performance, we calculated the hydrogen adsorption free energy (ΔG_{*H}) using the DFT method (Fig. 4c). Three models are employed in the DFT calculations (Fig. S20), the pristine Ni(111) surface, the Ni(111) surface covered with a carbon layer with 1 doped N (Ni@C−N), and the Ni(111) surface covered with a carbon layer with 2 doped N (Ni@C−2N). The Ni(111) surface

exhibits a low ΔG_{*H} of −1.00 eV, consistent with its experimentally observed overly strong hydrogen binding (Fig. 4c). Both Ni@C−N and Ni@C−2N show weakened hydrogen adsorption, suggesting that the capped carbon layer optimizes the ΔG_{*H} on Ni. Ni@C−N demonstrates a more optimized ΔG_{*H} of −0.23 eV than that of Ni@C−2N (−0.56 eV).

It suggests that the carbon shell with moderate N doping would give the best HOR activity, and too much N is not helpful for further improving the HOR activity. The high activity of Ni-
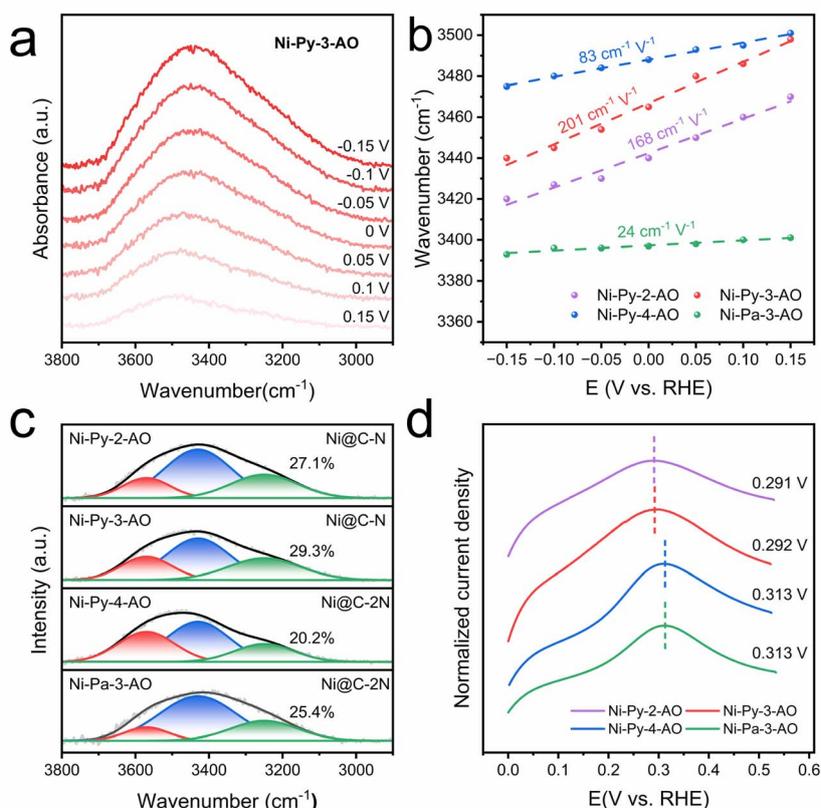

Fig. 5 (a) Electrochemical *in situ* ATR-SEIRAS of Ni-3-Py-AO. The background spectra were obtained at 0.2 V. (b) The Stark effect of Ni-Py-2-AO, Ni-Py-3-AO, and Ni-Py-4-AO. (c) Deconvolution results of the OH stretching vibration peak at 0 V. Three water peaks were identified at 3570 cm^{-1} (free water), 3430 cm^{-1} (weakly hydrogen-bonded water), and 3250 cm^{-1} (strongly hydrogen-bonded water). (d) The LSV curves of Ni-Py-2-AO, Ni-Py-3-AO, and Ni-Py-4-AO in 0.1 M Ar-saturated KOH.

Py-2-AO and Ni-Py-3-AO originates from their carbon shell with moderate N doping, which optimize the hydrogen binding.

The interfacial water structure is also important for the HOR activity, as it modulates the proton transfer kinetics.[37] The interfacial water structures are estimated by *in situ* ATR-SEIRAS performed between −0.15 and 0.15 V (Fig. 5a and S21). The progressive blue-shifting vibrational peaks with decreasing potential imply the influence of the electric field on the interfacial water structure. Ni-Py-3-AO exhibits the steepest Stark slope of 201 cm^{-1} V^{-1} (Fig. 5b), indicating the most pronounced voltage-dependent OH adsorption strength. We also deconvoluted the peak in the range of 3000–3600 cm^{-1} into three water configurations: strongly hydrogen-bonded water (3250 cm^{-1}), weakly hydrogen-bonded water (3430 cm^{-1}), and free water (3570 cm^{-1}) (Fig. 5c).[38,39] With more strongly hydrogen-bonded water, the hydrogen-bonding network is more complete, therefore promoting the HOR process. Ni-Py-3-AO shows the highest proportion of strongly hydrogen-bonded water (29.3%) compared with other catalysts, *i.e.*, Ni-Py-2-AO (27.1%), Ni-Py-4-AO (20.2%) and Ni-Pa-3-AO (25.4%). With the optimized hydrogen-bonding networks, the Volmer step is accelerated on Ni-Py-3-AO, thereby exhibiting superior HOR kinetics.

The interfacial water structures are correlated with the surface conditions of the catalysts. It has been reported that the adsorbed OH on the surface could induce the water to orient towards the O-down configuration, which is beneficial to connect with other water molecules as strongly hydrogen-bonded water. The OH adsorption strength is determined *via* cyclic voltammetry in Ar-saturated electrolyte. Ni-Py-3-AO shows a low OH^- adsorption at 0.292 V (Fig. 5d), suggesting its increased *OH coverage on the catalyst surface. The *OH induced the interfacial water, forming strong hydrogen-bond water, and thus promoting the HOR.

Conclusions

In conclusion, this work establishes ligand engineering as an effective strategy for developing high-performance Ni-based HOR catalysts. The nitrogen contents of the ligands control the doping level in the carbon shell, and the position of the functional group in the ligand regulates the metallic Ni content in the pyrolyzed catalysts. The Ni-Py-3-AO catalyst achieves high HOR activity and HEMFC performance. Mechanistic insights reveal that the enhanced kinetics originate from the optimized HBE derived from the carbon shell structure and a restructured interfacial water network. This study provides an efficient strategy for designing cost-effective catalysts for HEMFC devices.

Author contributions

Z. Z. supervised the project. Z. Z. and Y. C. conceived the project. Y. C. synthesized the catalysts and conducted material characterization. Y. C. and Q. L. performed the electrochemical tests. Y. C. and C. C carried out the *in situ* ATR-SEIRAS measurements. Y. C., H. W. and S. Z. assembled the HEMFC and evaluated its performance. A. Q. and Y. L. carried out the density functional theory calculations. Y. C., Y. W, J. W., W. Z. and Z. Z co-wrote the manuscript with input from all authors. All authors discussed the results and assisted during manuscript preparation.

Conflicts of interest

There are no conflicts to declare.

Data availability

All data associated with this study are available in the article and supplementary information (SI). Supplementary information is available. See DOI: https://doi.org/10.1039/d5sc09117a.

Acknowledgements

Notes and references

1 W. E. Mustain, M. Chatenet, M. Page and Y. S. Kim, *Energy Environ. Sci.*, 2020, **13**, 2805–2838.

2 J. Hyun and H.-T. Kim, *Energy Environ. Sci.*, 2023, **16**, 5633–5662.

3 B. P. Setzler, Z. Zhuang, J. A. Wittkopf and Y. Yan, *Nat. Nanotech.*, 2016, **11**, 1020–1025.

4 W. Ni, J. L. Meibom, N. U. Hassan, M. Chang, Y.-C. Chu, A. Krammer, S. Sun, Y. Zheng, L. Bai, W. Ma, S. Lee, S. Jin, J. S. Luterbacher, A. Schüler, H. M. Chen, W. E. Mustain and X. Hu, *Nat. Catal.*, 2023, **6**, 773–783.

5 J. Durst, A. Siebel, C. Simon, F. Hasché, J. Herranz and H. A. Gasteiger, *Energy Environ. Sci.*, 2014, **7**, 2255–2260.

6 J. Zheng, W. Sheng, Z. Zhuang, B. Xu and Y. Yan, *Sci. Adv.*, 2016, **2**, e1501602.

7 G. Zhao, J. Chen, W. Sun and H. Pan, *Adv. Funct. Mater.*, 2021, **31**, 2010633.

8 Y. Peng, C. Huang, M. Pan, X. Yue and S. Huang, *ACS Appl. Mater. Interfaces*, 2025, **17**, 49452–49460.

9 W. Sheng, M. Myint, J. G. Chen and Y. Yan, *Energy Environ. Sci.*, 2013, **6**, 1509–1512.

10 J. K. Nørskov, T. Bligaard, A. Logadottir, J. R. Kitchin, J. G. Chen, S. Pandelov and U. Stimming, *J. Electrochem. Soc.*, 2005, **152**, J23.

11 B. Huang, R. R. Rao, S. You, K. Hpone Myint, Y. Song, Y. Wang, W. Ding, L. Giordano, Y. Zhang, T. Wang, S. Muy, Y. Katayama, J. C. Grossman, A. P. Willard, K. Xu, Y. Jiang and Y. Shao-Horn, *JACS Au*, 2021, **1**, 1674–1687.

12 Y. Men, X. Men, P. Li, L. Li, X. Wang, X. Su, L. Zhang, S. Chen and W. Luo, *J. Am. Chem. Soc.*, 2025, **147**, 21672–21685.

13 A. H. Shah, Z. Zhang, Z. Huang, S. Wang, G. Zhong, C. Wan, A. N. Alexandrova, Y. Huang and X. Duan, *Nat. Catal.*, 2022, **5**, 923–933.

14 X. Wang, X. Liu, J. Fang, H. Wang, X. Liu, H. Wang, C. Chen, Y. Wang, X. Zhang, W. Zhu and Z. Zhuang, *Nat. Commun.*, 2024, **15**, 1137.

15 W. Sheng, A. P. Bivens, M. Myint, Z. Zhuang, R. V. Forest, Q. Fang, J. G. Chen and Y. Yan, *Energy Environ. Sci.*, 2014, **7**, 1719–1724.

16 M. Wang, H. Yang, J. Shi, Y. Chen, Y. Zhou, L. Wang, S. Di, X. Zhao, J. Zhong, T. Cheng, W. Zhou and Y. Li, *Angew. Chem., Int. Ed.*, 2021, **60**, 5771–5777.

17 Z. Zhuang, S. A. Giles, J. Zheng, G. R. Jenness, S. Caratzoulas, D. G. Vlachos and Y. Yan, *Nat. Commun.*, 2016, **7**, 10141.

18 W. Ni, A. Krammer, C. Hsu, H. M. Chen, A. Schüler and X. Hu, *Angew. Chem., Int. Ed.*, 2019, **58**, 7445–7449.

19 X. Zhao, X. Li, L. An, L. Zheng, J. Yang and D. Wang, *Angew. Chem., Int. Ed.*, 2022, **61**, e202206588.

20 X. Zhao, X. Li, L. An, K. Iputera, J. Zhu, P. Gao, R.-S. Liu, Z. Peng, J. Yang and D. Wang, *Energy Environ. Sci.*, 2022, **15**, 1234–1242.

21 X. Tian, R. Ren, F. Wei, J. Pei, Z. Zhuang, L. Zhuang and W. Sheng, *Nat. Commun.*, 2024, **15**, 76.

22 H. Su, W. Liao, S. Mo, H. Wang, Y. Cao, H. Yu and H. Wang, *Adv. Funct. Mater.*, 2025, e18373.

23 H. Sun, C. Li, L. Yang, Y. Han, X. Yu, C.-P. Li, Z. Zhang, Z. Yan, F. Cheng and M. Du, *Proc. Natl. Acad. Sci. U. S. A.*, 2023, **120**, e2308035120.

24 Y. Gao, Y. Yang, R. Schimmenti, E. Murray, H. Peng, Y. Wang, C. Ge, W. Jiang, G. Wang, F. J. DiSalvo, D. A. Muller, M. Mavrikakis, L. Xiao, H. D. Abruña and L. Zhuang, *Proc. Natl. Acad. Sci. U. S. A.*, 2022, **119**, e2119883119.

25 X. Wang, J. Fang, X. Liu, D. Wei, Y. Yin, H. Wei, J. Zhang, Y. Zhang, X. Zhang, W. Zhu and Z. Zhuang, *Appl. Catal., B*, 2023, **327**, 122442.

26 J. Liu, W. Yu, M. Wang, J. Gao, X. Cui and L. Jiang, *ACS Catal.*, 2025, **15**, 4110–4120.

27 J. Wang, X. Dong, J. Liu, W. Li, L. T. Roling, J. Xiao and L. Jiang, *ACS Catal.*, 2021, **11**, 7422–7428.

28 T. Wang, R. Jin, X. Wu, J. Zheng, X. Li and K. Ostrikov, *J. Mater. Chem. A*, 2018, **6**, 9228–9235.

29 J. He, L. Luo, J. Li, S. Chen, S. Yu, L. Zeng, Y. Wang and Y. Chen, *Angew. Chem., Int. Ed.*, 2025, **64**, e202423647.

30 J. He, S. Chen, S. Yu, L. Zeng, L. Luo, Y. Chen and Y. Wang, *J. Energy Chem.*, 2026, **113**, 246–254.

31 L. Zeng, T. Yuan, Y. Zhu, D. Wu, Q. Zhou and R. Tang, *Int. J. Hydrogen Energy*, 2023, **48**, 36353–36360.

32 W. Ni, T. Wang, F. Héroguel, A. Krammer, S. Lee, L. Yao, A. Schüler, J. S. Luterbacher, Y. Yan and X. Hu, *Nat. Mater.*, 2022, **21**, 804–810.

33 R. Ren, C. Ge, Q. Li, G. Wang, L. Xiao, J. Lu and L. Zhuang, *J. Power Sources*, 2023, **556**, 232439.

34 Y. Zhou, W. Yuan, M. Li, Z. Xie, X. Song, Y. Yang, J. Wang, L. Li, W. Ding, W.-F. Lin and Z. Wei, *Nat. Energy*, 2024, **9**, 1297–1309.

35 Y. Xu, W. Tu, B. Zhang, S. Yin, Y. Huang, M. Kraft and R. Xu, *Adv. Mater.*, 2017, **29**, 1605957.

36 V. Perazzolo, C. Durante, R. Pilot, A. Paduano, J. Zheng, G. A. Rizzi, A. Martucci, G. Granozzi and A. Gennaro, *Carbon*, 2015, **95**, 949–963.

37 P. Sebastián-Pascual, A. Herzog, Y. Zhang, Y. Shao-Horn and M. Escudero-Escribano, *Nat. Catal.*, 2025, **8**, 986–999.

38 L. Shen, B. Lu, Y. Li, J. Liu, Z. Huang-fu, H. Peng, J. Ye, X. Qu, J. Zhang, G. Li, W. Cai, Y. Jiang and S. Sun, *Angew. Chem., Int. Ed.*, 2020, **59**, 22397–22402.

39 K. Ataka, T. Yotsuyanagi and M. Osawa, *J. Phys. Chem.*, 1996, **100**, 10664–10672.